Vacuum 211 (2023) 111919

Contents lists available at ScienceDirect

Vacuum

journal homepage: www.elsevier.com/locate/vacuum

Density estimation of an ultrahigh-speed rarefied flow field based on force analysis of a pendulum sphere

Ning Han [a,b], Jin-Wen Cao [a,b,*], Xian Meng [a], Hong-Li Liu [a], Shao-Hua Zhang [a], He-Ji Huang [a,b]

[a] State Key Laboratory of High-Temperature Gas Dynamics, Institute of Mechanics, Chinese Academy of Science, No. 15 Beisihuanxi Road, Beijing, 100190, China
[b] School of Engineering Science, University of Chinese Academy of Science, Beijing, 100049, China

ARTICLE INFO

Handling Editor: L.G. Hultman

Keywords:
Density estimation
Pendulum sphere
Force analysis
Ultrahigh-speed rarefied flow

ABSTRACT

The similarity criterion for high speed or high enthalpy rarefied reaction flows is the binary scaling law, one of which is the product of the incoming flow density and the characteristic scale of the test model in a rarefied wind tunnel should be equal to that under the flight condition. This is to ensure that the ratio between the characteristic distance of the relaxation process and the characteristic length of the body is equal. However, in a rarefied wind tunnel, it is difficult to directly measure the flow density below 10^{-5} kg/m^3 using common methods due to the relatively high rarefied degree, an indirect density estimation method based on force analysis of a pendulum sphere was proposed in this study. The oscillation trajectory of the pendulum sphere under ultrahigh-speed rarefied flow conditions was recorded and the corresponding aerodynamic drag force acted on the sphere along the trajectory was analyzed, based on which the density distribution of the flow was then estimated combined with DSMC simulations. The obtained results show that in the present study, the flow is in under-expanded condition and the measured density sharply decreased from 10^{-6} kg/m^3 to 10^{-7} kg/m^3 at 140–170 mm from the nozzle outlet.

1. Introduction

Currently, the technological developments concerning the upper near space constitute an important issue due to the many applications in the near future. The design of transport vehicles for this space region is the most urgent step, while this region is also a completely new area due to the much more complex aerodynamic conditions, especially the aerodynamic loads on vehicles. Therefore, accurate ground prediction of rarefied aerodynamic characteristics is very important. The upper near space is in the transition flow region, where the real gas effect, rarefied gas effect and nonequilibrium effect are highly significant. Therefore, traditional experimental and computational methods based on continuous media are no longer fulfilling.

To obtain results comparable to those obtained in flight tests, ground experiments must satisfy similarity criteria. In addition to satisfying the Mach number and Reynolds number similarity criteria of continuous-medium wind tunnels, the similarity law for ultrahigh-speed rarefied gas flow extends to the binary scaling law, with two similar scales:

$$U_\infty, p_\infty L \tag{1}$$

This suggests that the ground flow field must simultaneously satisfy two similar conditions: (1) the same absolute velocity of the incoming flow to ensure a similar energy supply for the same chemical reactions; (2) the same product of the model characteristic scale and incoming flow density to ensure the same ratio of the characteristic distance of the relaxation process to the characteristic size of the object/flow field [1]. The general ground simulation conditions are difficult to satisfy this similar criterion.

In our previous work, we constructed a long-term ultrahigh-speed rarefied gas wind tunnel and effectively increased the incoming flow specific enthalpy via an optimized arc heating method to obtain tens of minutes-long 7 km/s nitrogen incoming flow conditions under an ambient pressure of 10^{-1} Pa [2]. The incoming gas velocity was calibrated using molecular tagging velocimetry [3,4].

Density measurement is equally important. Because of their nonintrusive property and the lack of flow field disturbance during measurement, optical techniques are popular among conventional wind tunnel density measurement methods. For rather high density flows, the shadow method, schlieren method, and interferometric method are the most frequently used optical density field measurement techniques

* Corresponding author. State Key Laboratory of High-Temperature Gas Dynamics, Institute of Mechanics, Chinese Academy of Science, No. 15 Beisihuanxi Road, Beijing, 100190, China.
E-mail address: caojinwen@imech.ac.cn (J.-W. Cao).

https://doi.org/10.1016/j.vacuum.2023.111919
Received 23 July 2022; Received in revised form 12 February 2023; Accepted 15 February 2023
Available online 22 February 2023

[5–8]. Although the shadow method is simple to use, it is not appropriate for quantitative measurement. To quantitatively measure the density the schlieren method should be utilized [9]. The background oriented schlieren methodology and the rainbow schlieren deflectometry approach were recently developed [5,10,11]. In a blowdown wind tunnel, Leopold et al. reported using a background-oriented schlieren technique termed colored background oriented schlieren (CBOS) that obtained densities between 0.4 and 1.4 kg/m^3 [12]. For high speed flow, optical interferometry is the most often employed quantitative density measurement technique [13–15]. In a hypersonic wind tunnel with a Mach number of 10.29, Song et al. reconstructed the density distributions of an axially symmetric flow field and found that the density ranged from 3.2×10^{-2} to 4.6×10^{-2} kg/m^3 [15]. On the other hand, the density in ultrahigh-speed rarefied gas flow is too low to be measured using traditional optical interferometry. In supersonic/hypersonic low-density wind tunnels, glow discharge visualization has recently been employed as a straightforward visualization technique [16–19]. However, this method cannot obtain quantitative density results, and the discharge in this method influences the flow properties. The method based on measurement of the fluorescence excited by an electron beam [20–24] is a feasible way to obtain the density of a rarefied gas; however recent experimental works indicate that measurable densities are still high, actually approaching 10^{-5}–10^{-4} kg/m^3 [24,25]. For even lower density flows, there is no good means to measure the flow density directly. Our previous work showed that when the chamber pressure was below 10 Pa, the laser-induced fluorescence technique [26–28] could not generate a strong enough fluorescence signal for detection and therefore density estimation could not be performed.

Flow field parameters can also be characterized using simple-shape bodies, since their behavior has been relatively well studied in both continuous medium-flow fields and rarefied flow fields. Studies have used a flat plate or a sphere to study the shock wave structure [29–31], the upstream density disturbance effect [32,33], and surface heating by hypersonic low-density flow [34]. By using a pendulum sphere model in a hypersonic rarefied wind tunnel of the Japan Aerospace Exploration Agency, the sphere displacement caused by aerodynamic forces was measured, and the test flow structure was carefully examined together with numerical simulations [35,36].

Aiming at the difficulty of direct density measurement at low density conditions, an indirect density estimation method for ultrahigh-speed rarefied flow fields using a small pendulum sphere was proposed in this work. The oscillation trajectory of the pendulum sphere model was experimentally observed in ultrahigh-speed rarefied flow, and the corresponding aerodynamic drag force acting on the sphere along the trajectory was analyzed. The aerodynamic drag force can also be calculated using the direct simulation Monte Carlo (DSMC) method, the results which were compared to the experimental results so as to verify the feasibility of the proposed method. The aerodynamic force acting on the sphere is related to the flow density, flow velocity, etc. Based on force analysis of the pendulum sphere, the density distribution was then estimated in combination with DSMC simulations. In this study, the proposed indirect method can quantitatively provide the distribution of the ultrahigh-speed rarefied flow field.

2. Model, methods, and theory

2.1. Ultrahigh-speed rarefied wind tunnel

Experiments were performed in a long-term rarefied gas wind tunnel at the Institute of Mechanics (Fig. 1). The continuous rarefied wind tunnel is a rarefied wind tunnel with a high enthalpy and an ultrahigh speed [2,37].

A schematic of the experimental system is shown in Fig. 2. The rarefied gas wind tunnel is composed of several parts, including a plasma heating generator, a test vacuum chamber, a vacuum pumping system, a parameter measurement system, and a corresponding power assist system.

Fig. 1. Long-term ultrahigh-speed rarefied gas wind tunnel at the Institute of Mechanics, Chinese Academy of Sciences.

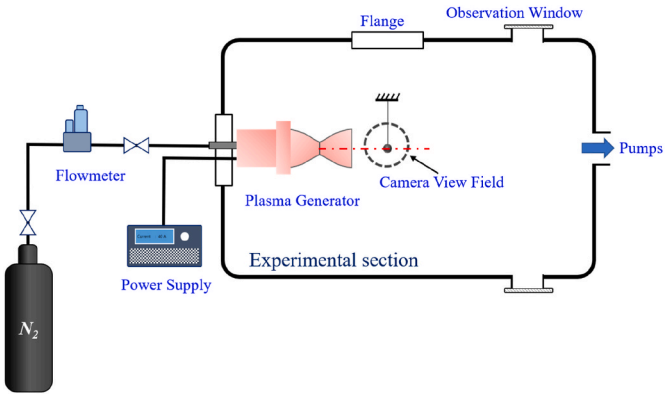

Fig. 2. Schematic of the experimental system.

The classical plasma heating generator injects energy into the incoming gas and accelerates the gas into the test chamber through a unique structure, i.e., an optimized de Laval nozzle, to obtain the required uniform high-speed and high-enthalpy gas flow conditions [38,39]. In this study, the addition of differential pumping near the throat, using a separate stage vacuum pump to bypass low-enthalpy exhaust gas near the throat, increase the average enthalpy of the accelerated expansion gas flow in the nozzle expansion section and reduces the gas flow into the main vacuum chamber, which can reduce the pumping burden of the vacuum pumping system. The corresponding plasma generator nozzle exit diameter is 20 mm.

A long-term rarefied gas wind tunnel must maintain a high vacuum degree under the condition of supplying incoming flow gas. The vacuum pumping system in use here includes molecular pumps, cryogenic pumps, and a pre-stage rough pumping unit that can provide the vacuum chamber with the requisite back pressure condition to satisfy the Knudsen number similarity requirements (*Kn*). The pumping speed of the vacuum pumping unit of the existing long-term rarefied gas wind tunnel can reach 54,000 L/s. To keep the working pressure at 10^{-1} Pa, the wind tunnel currently has a maximum flow rate of 0.1 g/s.

The parameter measurement system monitors the operating state of the entire system and collects experimental data. The power assist system supplies the whole system with cooling water, electricity, and gas.

In the experiments, the background pressure was monitored by pressure sensors covering the pressure ranges of concern and reached a steady value since the injected gas flow was controlled by a flowmeter.

To exclude the influence of residual gas on the experiments, the vacuum chamber of the wind tunnel was pumped to a pressure of approximately 10^{-3} Pa before injecting the working gas.

In the pendulum sphere experiment, the working gas was pure nitrogen with a gas flow rate of 83 mg/s. The power input of the plasma generator was approximately 3 kW. The real ambient back pressure was 0.6 Pa.

2.2. Sphere model

The pendulum sphere model should adopt high roundness dimensional accuracy to ensure effective measurement of the density of the ultrahigh-speed rarefied flow field. The selection of suspension wire should be as light, thin, and flexible as possible on the basis of ensuring sufficient strength to reduce the interference of the suspension wire in the flow field and the additional force generated on the sphere model.

The primary body of the suspension wire sphere system was a bearing steel spherical model with a diameter of 5 mm, and its mass was 0.524 g. The suspension wire was a silver wire with a diameter of 0.1 mm that was spot-soldered onto the surface of the spherical model. The mean free path of nitrogen molecules is on the order of centimeters when the ambient pressure is 10^{-1} Pa, so the choice of a 0.1 mm suspension wire is feasible.

The system of the suspended wire sphere and the forces actting on it are schematically depicted in Fig. 3. The x- and z-directions are the axial directions, and the y- and r-directions are the radial directions. The sphere underwent a simple pendulum motion in the experiment as a result of the combined action of gravity, i.e., mg, the suspension wire tension, i.e., $T(x)$, and the aerodynamic force, i.e., $F(x)$. The initial position z_0 of the sphere was 103 mm, and the position of the nozzle outlet was $z = 0$. The trajectory of the sphere was captured with a video camera at a frame rate of 25 fps. Under the same aerodynamic conditions, increasing the length of the suspension wire can help improve the image resolution accuracy [40]. Considering the above factors, the length of the suspension wire L in the experiment was set to 430 mm.

2.3. DSMC method

The DSMC method, in which molecules are the object of study, is a reliable tool for analyzing hypersonic rarefied gas flows [41]. An important factor determining the reliability and accuracy of the simulation results obtained using this method is the grid scheme. Based on the position element algorithm proposed by Bird [42,43], a new version of the position element algorithm was developed [44,45], involving a hybrid grid scheme and a structureless meticulous description of the object surface to ensure high accuracy of the calculation results [46].

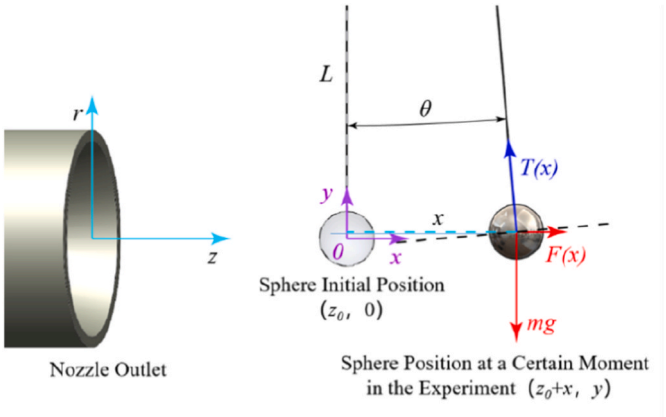

Fig. 3. Schematic diagram of the suspension sphere system and forces acting on the sphere.

Hypersonic spherical disturbances in the slipstream, transition, and free molecular flow regions were simulated using a common program of position elements that included a new surface element representation. The calculation results were good agreement with the experimental data, indicating that the new DSMC position element algorithm with a hybrid grid scheme could effectively and accurately simulate rarefied gas flows and could effectively ensure the accuracy of aerodynamic calculations [47]. However, due to the notably challenging nature of ground test implementation, the data needed to compare DSMC and ultrahigh-speed rarefied flow field results are constrained. The flow field parameters acquired from DSMC numerical simulations must be compared to test results from experiments [48].

The new version of the DSMC method was used in this study. The studied problem is roughly categorized as an axisymmetric problem. Because the particle velocity at the outlet is very high and the expansion angle of the core air flow to both sides is small, an area not far from the rear of the sphere as the horizontal right boundary, which will not affect the flow field distribution in the direction of the incoming flow. The width of the left boundary is chosen as 5 times the nozzle diameter. Instead of simulating the flow in the pipe inside the nozzle, the left boundary is set to the nozzle output interface. The lower boundary is set to the axis of the nozzle. This paper mainly focuses on the force acting on the sphere in the flow field. The degree of ionization or temperature of the incoming gas has little influence on the aerodynamic force. Therefore, the particles in this simulation are all regarded as neutral particles.

To ensure a more realistic simulation of the surface of the sphere, the grids are selected as unstructured grids. The grid density steadily decreases from the nozzle outlet to the right boundary and is higher on the sphere surface and close to the nozzle exit. There are approximately 100,000 grids in total. The average number of molecules is approximately 150 to improve the simulation accuracy, and under normal circumstances, there are approximately 15 million simulated molecules overall. The characteristic scale of the grid is approximately 1/4 of the local mean free path. According to the requirements of the DSMC algorithm, the time step should be smaller than the smallest mean collision time of the incoming flow molecules. The mean collision time upstream of the sphere is 2.1×10^{-6} s, whereas the characteristic time step is 2.0×10^{-7} s, which is about one order of magnitude smaller. The particle collision model is selected as the variable hard sphere (VHS) model. Since nitrogen is present in the entering flow, the temperature exponent of the coefficient of viscosity can be taken as 0.74. The reflection condition of the surface of the small sphere is treated as diffuse reflection, and the initial temperature of the wall is set to 300 K.

In this study, velocity analysis was used to validate the feasibility of using the DSMC method under ultrahigh-speed rarefied gas flow conditions. The ultrahigh-speed rarefied gas flow velocity at $z = 30$ mm was measured using MTV. The results are shown in Fig. 4. The radial velocity distribution obtained from the experimental measurements reveals that the ultrahigh-speed rarefied gas velocity reached approximately 5 km/s near the center of the nozzle, and the gas velocity was nearly symmetric along the radial direction. The gas flow pattern at the ultrahigh-speed rarefied facility conforms to the flow pattern of free jets, in which the gas jetted from the nozzle constantly expands and high-speed gas spreads along the radial direction of gas flow [49–52]. Meanwhile, the velocity distribution at the experimental measurement position was calculated using the DSMC method, and the numerical results were also consistent with this pattern. The velocity results between the experimental measurements and numerical simulations agreed. This numerical simulation method could be applicable under the experimental conditions in this article.

With the use of the velocity and temperature measured experimentally as initial conditions, the aerodynamic force acting on the sphere in the ultrahigh-speed flow field could be determined. By comparing the aerodynamic forces obtained by image analysis with those obtained by the DSMC method, the feasibility of using the indirect method to estimate the density was verified. Then, the ultrahigh-speed flow field

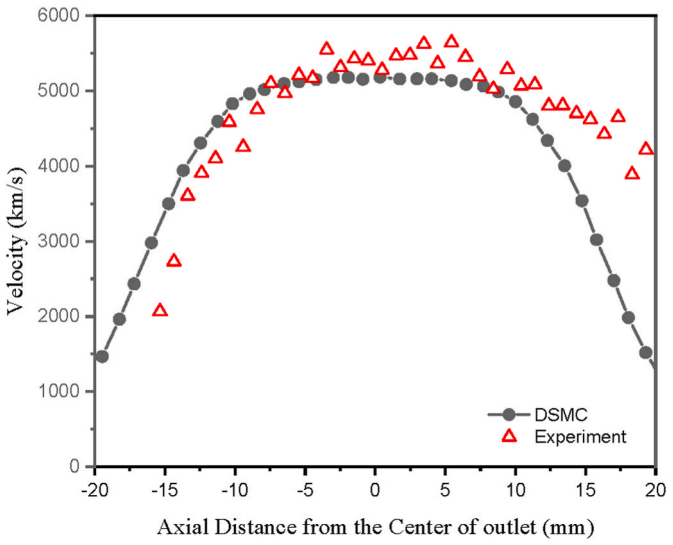

Fig. 4. Velocity distribution in the experiment and simulations.

density distribution was estimated by combining the results obtained by experimental aerodynamic force with the flow parameters obtained by the DSMC method.

2.4. Density estimation

The aerodynamic force on the sphere $F(x)$ was thought to act in only one direction—axially—and depend on the position of the sphere. The mass of the silver suspension wire with a length of 430 mm and a diameter of 0.1 mm accounted for approximately 7% of the mass of the sphere and was ignored in this study. According to Newton's law, the equation of the sphere motion along the direction perpendicular to the suspension wire can be approximated as:

$$F(x)\cos\theta - mg\sin\theta = m\ddot{x} \tag{2}$$

where θ is the deflection angle of the suspension wire.

In addition,

$$\sin\theta = \frac{x}{L} \tag{3}$$

Therefore, the following can be obtained:

$$F(x) = \frac{m\ddot{x} + mg\frac{x}{L}}{\sqrt{1-\frac{x^2}{L^2}}} \tag{4}$$

The magnitude of the aerodynamic force acting on the sphere in an ultrahigh-speed rarefied gas flow is closely related to parameters such as the flow velocity v, flow density ρ, and drag coefficient C_d:

$$F(x) = \frac{1}{8}\pi d^2 C_d \rho(x) v^2 \tag{5}$$

where $\rho(x)$ is the incoming flow density distribution of interest in this study. Equation (5) indicates that the aerodynamic force is proportional to the drag coefficient (i.e., C_d) and square of the velocity (i.e., v^2). The drag coefficient C_d is a key parameter for evaluating the magnitude of the aerodynamic force acting on the sphere. Within the hypersonic range, C_d is influenced by the ratio of the sphere wall temperature to the incoming temperature, and the effect of the temperature is slight if the sphere wall temperature does not greatly exceed the incoming flow temperature [53]. The influence of temperature on the drag coefficient is minimal because there was little evidence in this investigation that the sphere wall temperature was significantly greater than the incoming flow temperature. As a result of the minor impact of the temperature on the drag coefficient, while computing the incoming flow density at the same aerodynamic level, the temperature has a minor impact while the velocity has a substantial impact.

Reference [54] provided a simple expression of the drag coefficient based on the Mach number (M_a) and Reynolds number (R_{eD}, i.e., the Reynolds number of free incoming flow based on the sphere diameter as the characteristic length, with a magnitude ranging from 0.01 to 1 in the experimental conditions) under hypersonic rarefied flow conditions:

$$C_d = 0.9 + \frac{1}{2}\frac{Ma}{\sqrt{R_{eD}}} \tag{6}$$

According to the definitions of the Mach number and Reynolds number, the aerodynamic force can be expressed by the following equation:

$$F(x) = \frac{\pi}{8}v^2 d^2\left(0.9 + \frac{1}{2}\sqrt{\frac{\mu v}{\gamma RTd\rho(x)}}\right)\rho(x) \tag{7}$$

where γ is the gas specific heat ratio, R is the gas constant, T is the incoming flow temperature, and μ is the dynamic viscosity of the gas.

Combining Equations (4) and (5) yields the following:

$$\rho(x) = \left(\frac{-ab + \sqrt{a^2b^2 + 3.6aF(x)}}{1.8a}\right)^2 \tag{8}$$

where:

$$a = \frac{1}{8}\pi v^2 d^2 \tag{9}$$

$$b = \frac{1}{2}\sqrt{\frac{\mu v}{\gamma RTd}} \tag{10}$$

Following the experiment, successive frames was intercepted from the videos, and image processing was used to determine the position of the sphere at various time points $x(t)$. In this study, two methods were used to analyze the acceleration of the sphere at different positions during experimental data processing. 1) The sphere displacement and time interval between adjacent frames were directly used to determine the sphere acceleration. This method may yield a large error because the frame rate of the ordinary camera used in the current experiment reached only 25 fps, and the temporal resolution was insufficient. 2) The experimental $x(t)$ data were fitted, and the fitting relationship was used to derive the analytical x'' value. The problem with this method lies in the selection of the fitting equation. An unreasonable fitting relationship may yield a nonphysical independent variable–dependent variable relationship that cannot be extrapolated. However, interpolation could be possible within the range of independent variables measured experimentally. After obtaining x'', $F(x)$ was determined via substitution into Equation (2). Then, substitution into Equation (8) yielded $\rho(x)$.

3. Results and discussion

3.1. Aerodynamic evaluation

Photographs of the initial sphere position and the position at a moment in the blowing process are shown in Fig. 5(a) and (b), respectively.

Fig. 6 shows a series of positions during sphere oscillation within approximately one oscillation cycle obtained via image analysis. A circular fit was adopted for this series of positions fit, and the fitting equation can be expressed as follows:

$$\left(x + 1.5\times10^{-6}\right)^2 + (y - 0.4291)^2 = 0.4291^2 \tag{11}$$

The fitted oscillation radius was 0.4291 m, which agrees well with the actual hanging wire length, indicating that the accuracy of the fitting

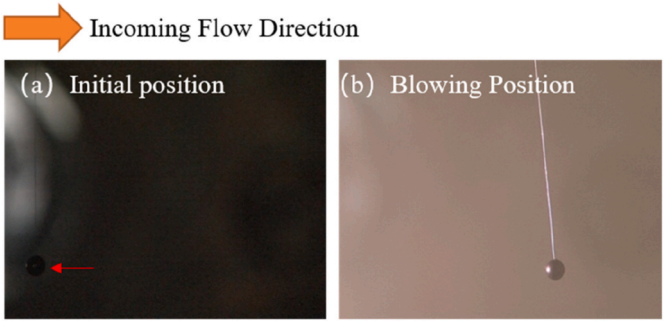

Fig. 5. (a) Initial position of the sphere; (b) photograph of the blowing position.

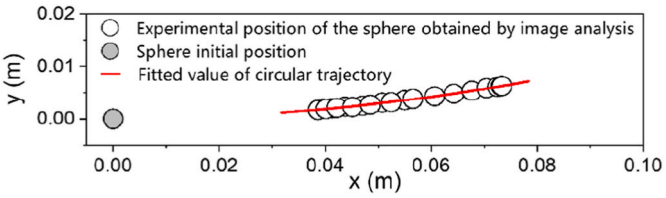

Fig. 6. Series of sphere positions and fitting curve obtained via photograph image analysis.

relationship meets the requirements when the sphere position is determined in the image processing software.

The displacement of the sphere along the x-axis over time is shown in Fig. 7, and the fitting curve obtained by a trigonometric function fitting relationship can be expressed as follows:

$$x(t) = 0.05605 - 0.001165\cos(5.966t) - 0.01733\sin(5.966t) \quad (12)$$

The figure shows that under the condition of an incoming plume, the sphere followed a simple pendulum-like movement trajectory, and the swing period reached approximately $2\pi/5.966 = 1.05s$.

As previously mentioned, the direct and fitting methods were used to determine x' and x''. Then, the corresponding $F(x)$ value could be obtained. x' and x'' were calculated with the fitting relationship of $x(t)$, namely, Equation (12), as follows:

$$x' = 0.00695\sin(5.966t) - 0.1034\sin(5.966t) \quad (13)$$

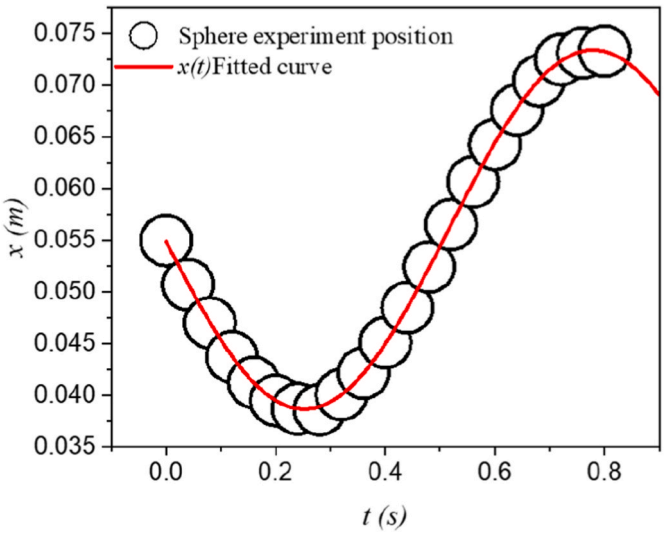

Fig. 7. Measured positions and fitting curve of $x(t)$.

$$x'' = 0.041466\cos(5.966t) + 0.616829\sin(5.966t) \quad (14)$$

$F(x)$ corresponding to the fitting relationship could be obtained with Equation (5).

Fig. 8(a)–(c) show a comparison of the velocity, acceleration, and aerodynamic force distributions of the sphere obtained by the two methods. The abovementioned figures show that the deviation between the direct and proposed methods increased with the number of derivatives, which is mainly attributed to the large time interval between adjacent frames when the direct method is used, and the selection of time points and space points corresponding to the average value of the corresponding physical quantities easily generates deviations. In contrast, the fitting method is equivalent to encrypting interpolation points within the experimental points, which could improve the spatiotemporal resolution accuracy in a mathematical sense. In general, the change trends of the physical quantities obtained with the fitting method were similar to those obtained with the direct method in the range of experimental data.

As shown in Fig. 8(a), because of the reciprocal oscillation of the pendulum sphere, when the pendulum sphere is at the same position but moving in opposite directions, the velocity should be equal in magnitude but opposite in direction. The velocity reached zero at the nearest and farthest oscillation positions. The result obtained with the proposed fitting method was more reasonable. Under the experimental conditions, the maximum linear velocity of the swinging sphere reached 0.1 m/s.

The position where the sphere acceleration reached zero in Fig. 8(b) should represent the position of equilibrium between the gravitational component and the aerodynamic component. Under the existing experimental conditions, the equilibrium position was basically located at the center of the pendulum sphere swing trajectory, suggesting that although the aerodynamic force changed along the x-direction, the change in this value was smaller than the sphere gravity. Based on the distribution shown in Fig. 8(c), this could be confirmed.

As shown in Fig. 8(c), for $z_0 = 103$ mm, the axial aerodynamic force acting on the 5-mm diameter sphere ranged from 0.79–0.57 mN at 140–170 mm from the nozzle outlet and decreased with increasing axial distance.

$F(x)$ was also obtained with the abovementioned version of the DSMC method using the flow field velocity measured by MTV and the measured temperature as the initial calculation conditions. The temperature was deduced from the vibration-rotation leap spectral bands of the NH ($A^3\Pi - X^3\Sigma$) nitrogen-hydrogen free radical, resulting in a value of approximately 4700 K in the plasma plume. The calculated aerodynamic force was approximately 0.51 mN. Compared to the force deduced based on the experimental positions of the sphere, there was a deviation in the magnitude. This difference was acceptable because the force determined by the numerical approach is the force along the central axis.

3.2. Quantitative density estimation

Based on the $F(x)$ data depicted in Fig. 8, the flow density could be estimated using Equation (8)~(10). The plasma plume temperature was determined based on the rotation temperature mentioned earlier, i.e., 4700 K. The viscosity at the corresponding temperature could be retrieved from a table of nitrogen transport properties [55]. The velocity was provided by DSMC simulation. The densities under the corresponding experimental conditions were estimated, as shown in Fig. 9, and the density ranged from 10^{-6}–10^{-7} kg/m^3 at 140–170 mm from the nozzle outlet.

As shown in Fig. 9, density estimation was carried out in the temperature range of 2000–4000 K and in the velocity range from 2–5 km/s. Preliminary numerical simulations and experimental measurements indicated that the average nozzle outlet temperature ranged from approximately 2000–4000 K [56–58]. As shown in Fig. 9, whereas the

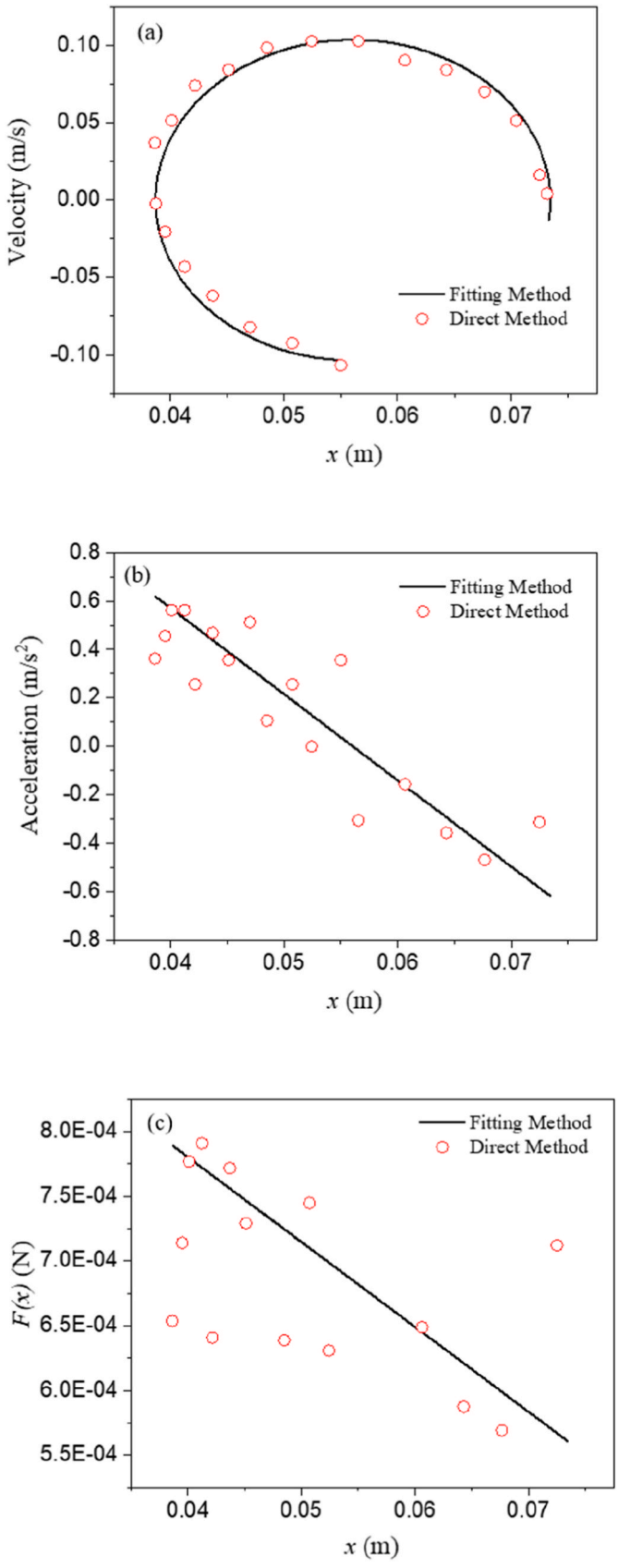

Fig. 8. Velocity, acceleration and aerodynamic force of the sphere model with changing position obtained with the direct and fitting methods.

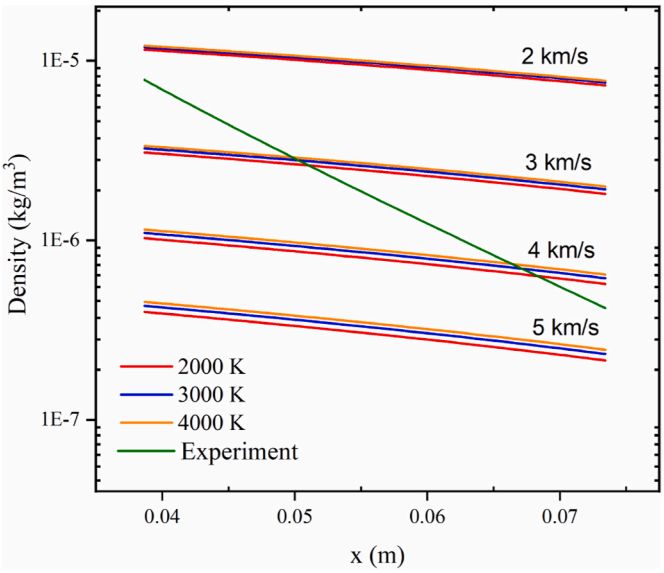

Fig. 9. Estimation of the flow density distribution within different temperature and velocity ranges.

density was significantly impacted by velocity, temperature only had a minor impact. This is consistent with the previous theoretical analysis.

The density distribution with a sphere obtained with the DSMC method is shown in Fig. 10. When a sphere was present in the flow field, a density disturbance occurred near the sphere. The density distribution obtained with the numerical simulation method was on the same order of magnitude as that obtained with the indirect method based on the experimental conditions.

Under the experimental conditions described in this study, the incoming flow density in the ultrahigh-speed rarefied wind tunnel ranged from 10^{-6}–10^{-7} kg/m^3 at a distance of 140–170 mm from the nozzle outlet. The current rarefied gas wind tunnel design operates in an under-expanded state; thus, with increasing axial distance, the gas further expands, leading to a decrease in the incoming flow density [59].

3.3. *Effect of the aerodynamic force gradient on the pendulum oscillation*

From the aerodynamic force results shown in Fig. 8(c), the aerodynamic force is obviously not uniform along the oscillation trajectory of the sphere. Therefore, the temporal oscillation of the pendulum sphere is not a perfect sine function, which can be observed from the

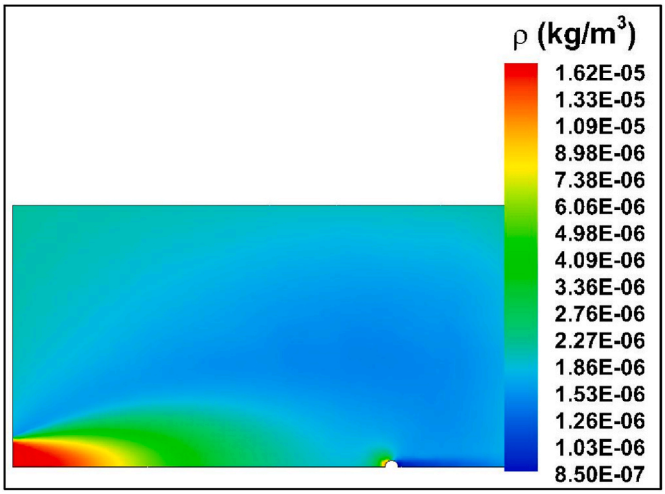

Fig. 10. Density distribution with a sphere obtained via the DSMC method.

velocity results calculated by the direct method as shown in Fig. 8(b). Moreover, the observed oscillation period of the pendulum sphere is significantly smaller than the traditional theoretical value, i.e.,

$$T = 2\pi\sqrt{\frac{L}{g}} \tag{15}$$

which gives a value of approximately 1.316 s Where g is the gravity acceleration, i.e. 9.8 m/s^2. Therefore, the fitting function of equation (12) is approximate. However, the approximation is sufficiently precise for the purpose of these experiments since the discrepancy of the fitting curve from the directly calculated results is small, as shown in Fig. 8(b). Moreover, the measured force gradient is consistent with the decrease in the observed oscillation period from the uniform flow value, which verifies the feasibility of the method. The subsequent section provides an analysis of the effect of the force gradient.

The deflection angle at the equilibrium position of the pendulum is defined as θ_0, where the net force on the sphere is zero, and θ is redefined as the deflection angle in relation to θ_0, as shown in Fig. 11. The polar coordinates (e_r, e_θ) are used. Since the motion in the radial direction is constrained by the wire, only the force components projected along the e_θ axis will act. Using these denotations, equation (2) is rewritten as

$$mL\frac{d^2\theta}{dt^2} = -G\sin(\theta+\theta_0) + F_d(\theta+\theta_0)\cos(\theta+\theta_0) \tag{16}$$

Using the facts that $\theta \ll \theta_0$ and $\theta \ll 1$, and expanding the aerodynamic force at the equilibrium position,

$$F(\theta+\theta_0) = F(\theta_0) + \left.\frac{dF}{d\theta}\right|_{\theta=\theta_0}\theta + \mathrm{O}(\theta^2) \approx F_0 + F_\theta\theta \tag{17}$$

where F_0 is the aerodynamic force at equilibrium position $\theta_0 \approx 0.1106^\circ$, which is approximately 0.65 mN as shown in Fig. 8. F_θ is the angular force gradient at the equilibrium position, and can be averaged according to the aerodynamic force distribution shown in Fig. 8 (c), i.e.,

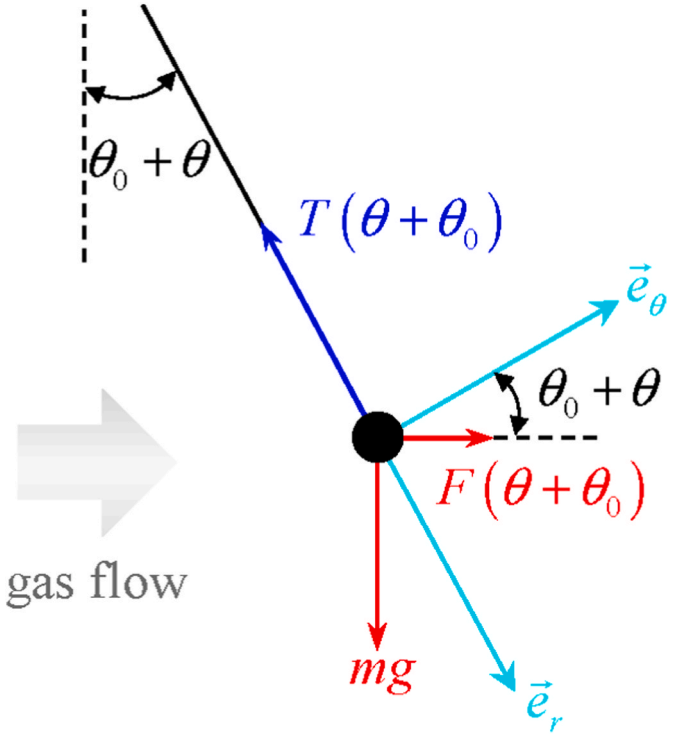

Fig. 11. Schematic illustration of the forces acting on the pendulum sphere.

$$F_\theta \approx \frac{F_{\max} - F_{\min}}{\theta_{\max} - \theta_{\min}} \approx -3.728mN \tag{18}$$

Combining equation (16) ~ (18), the oscillation motion can be described as

$$mL\frac{d^2\theta}{dt^2} = -[(G - F_\theta)\cos\theta_0 + F_0\sin\theta_0]\theta - F_\theta\sin\theta_0\theta^2 \tag{19}$$

Omitting the high-order small quantity related to θ^2, the oscillation period of the pendulum sphere in the rarefied gas flow should be

$$T = 2\pi\sqrt{\frac{mL}{(G - F_\theta)\cos\theta_0 + F_0\sin\theta_0}} \approx 0.997\mathrm{s} \tag{20}$$

This result agrees well with the experimentally acquired value, 1.05 s, and the deviation of approximately 0.053 s is nearly equal to the temporal resolution of the camera, i.e., 0.04 s. In equation (19), the contribution from the aerodynamic force, i.e., $F_0\sin\theta_0$, is trivial since it is much smaller than the other term. Therefore, the aerodynamic force gradient determines the pendulum sphere oscillation period, and the fitting method is actually a first-order approximation of the pendulum motion and has good precision for calculating the aerodynamic forces along the trajectory.

4. Conclusion

Aiming at the difficulty of direct density measurement at low density conditions, an indirect density measurement method for high-velocity rarefied flow is proposed using a small pendulum sphere. Making use of the relationship between the aerodynamic force on the sphere and the flow density, the density could be estimated with the local velocity information. In our studies, the local velocity was obtained through the DSMC numerical calculation with input initial conditions from MTV experiments.

Under the incoming pure nitrogen plasma flow conditions, the aerodynamic force deduced from the image sequences of a 5-mm diameter sphere was less than 1 mN but could be effectively distinguished and agreed with the DSMC calculated results. Based on these results, the estimated value of the density ranged from 10^{-6}–10^{-7} kg/m^3 at a distance of 140–170 mm from the nozzle outlet.

The errors in this method mainly originated from the low frame rate of the camera, which could be improved with a high-speed camera, and from the temporal oscillation of the pendulum sphere. The oscillation of the sphere was not a perfect sine function with time because of the gradient of the aerodynamic force on the sphere due to the nonuniformity of the flow parameters. An analysis of the gradient effect on the sphere oscillation was conducted, and the measured aerodynamic force distribution along the trajectory was consistent with the observed motion of the sphere, especially the predicted oscillation period, which agreed well with the observed value. These results demonstrate that the proposed method is a feasible way to indirectly estimate the density of high-velocity rarefied gas flow.

CRediT authorship contribution statement

Ning Han: Visualization, Methodology, Investigation, Formal analysis, Data curation, Writing – original draft, Writing – review & editing. **Jin-Wen Cao:** Writing – review & editing, Methodology. **Xian Meng:** Investigation. **Hong-Li Liu:** Software. **Shao-Hua Zhang:** Resources. **He-Ji Huang:** Visualization, Methodology, Funding acquisition.

Declaration of competing interest

The authors declare that they have no known competing financial interests or personal relationships that could have appeared to influence the work reported in this paper.

Data availability

Data will be made available on request.

Acknowledgments

This work was supported by the Strategic Priority Research Program of the Chinese Academy of Sciences (Grant No. XDA17030100), the National Natural Science Foundations of China under Grant 11735004 and Grant 11575273, and the Hainan Province Science and Technology Special Fund (Grant No. ZDKJ2019004).

References

[1] C. Shen, Rarefied Gas Dynamics: Fundamentals, Simulations and Micro Flows, Springer, Berlin, Heidelberg, 2005.
[2] W. Pan, X. Meng, H. Huang, C. Wu, Producing ultra-high-speed nitrogen jets by arc heating in a low-pressure chamber, Theor. Appl. Mech. Lett. 6 (2016) 60–63, https://doi.org/10.1016/j.taml.2015.12.003.
[3] S. Zhang, X. Yu, H. Yan, H. Huang, L. Liu, Molecular tagging velocimetry of NH fluorescence in a high-enthalpy rarefied gas flow, in: A. Sasoh, T. Aoki, M. Katayama (Eds.), 31st International Symposium on Shock Waves, Springer International Publishing, Cham, 2017, pp. 377–384.
[4] J. Cao, H. Huang, W. Pan, X. Meng, C. Wu, Specific signal imaging velocimetry for rarefied plasma flows, Exp. Fluid 61 (2020) 247, https://doi.org/10.1007/s00348-020-03080-9.
[5] G.S. Settles, M.J. Hargather, A review of recent developments in schlieren and shadowgraph techniques[J], Meas. Sci. Technol. 28 (2017), 042001, https://doi.org/10.1088/1361-6501/aa5748.
[6] A. Hirschberg, Schlieren and shadowgraph techniques: visualizing phenomena in transparent media: G.S. Settles, Eur. J. Mech. B Fluid 21 (4) (2002) 493–494, https://doi.org/10.1016/s0997-7546(02)01191-3.
[7] D. Tobin Jesse, M.J. Hargather, Quantitative schlieren measurement of explosively-driven shock wave density, temperature, and pressure profiles, Propellants, Explos. Pyrotech. 41 (2016) 6, https://doi.org/10.1002/prep.201600097.
[8] C. Söller, R. Wenskus, P. Middendorf, et al., Interferometric tomography for flow visualization of density fields in supersonic jets and convective flow, Appl. Opt. 33 (14) (1994) 2921, https://doi.org/10.1364/AO.33.002921.
[9] R. Mariani, B. Zang, H.D. Lim, et al., A Comparative Study on the Use of Calibrated and Rainbow Schlieren Techniques in Axisymmetric Supersonic Jets, Flow Measurement and Instrumentation, 2019, https://doi.org/10.1016/j.flowmeasinst.2019.01.007.
[10] R. Mariani, H.D. Lim, B. Zang, et al., On the application of non-standard rainbow schlieren technique upon supersonic jets, J. Visual 23 (3) (2020) 383–393, https://doi.org/10.1007/s12650-020-00637-y.
[11] M. Raffel, Background-oriented schlieren (BOS) techniques, Exp. Fluid 56 (3) (2015) 60, https://doi.org/10.1007/s00348-015-1927-5.
[12] F. Sourgen, F. Leopold, D. Klatt, Reconstruction of the density field using the colored background oriented schlieren technique (CBOS), Opt Laser. Eng. 50 (1) (2012) 29–38, https://doi.org/10.1016/j.optlaseng.2011.07.012.
[13] S. Sugawara, S. Nakao, Y. Miyazato, et al., Quantitative flow visualization of slightly underexpanded microjets by Mach–Zehnder interferometers, Flow, Turbul. Combust. (2020) 3–4, https://doi.org/10.1007/s10494-020-00211-4.
[14] H. Thayyullathil, H. Langoju, R. Padmaram, et al., Three-dimensional Optical Tomographic Imaging of Supersonic Jets through Inversion of Phase Data Obtained through the Transport-Of-Intensity Equation, Applied Optics, 2004, https://doi.org/10.1364/ao.43.004133.
[15] Y. Song, B. Zhang, A.Z. He, Algebraic iterative algorithm for deflection tomography and its application to density flow fields in a hypersonic wind tunne, Appl. Opt. 45 (3 1) (2006) 8092–8101, https://doi.org/10.1364/AO.45.008092.
[16] A.E. Ieshkin, A.V. Danilov, I.E. Chernysh, et al., Visualization of supersonic flows with bow shock using transversal discharges, J. Visual 22 (4) (2019) 741–750, https://doi.org/10.1007/s12650-019-00565-6.
[17] A.E. Ieshkin, A.V. Danilov, I.E. Chernysh, et al., Visualization by discharge illumination technique and modification by plasma actuator of rarefied Mach 2 airflow around a cylinder, Meas. Sci. Technol. 24 (2013), 065401, https://doi.org/10.1007/s12650-019-00565-6.
[18] P. Palm, R. Meyer, E. Plonjes, J.W. Rich, I.V. Adamovich, Nonequilibrium radio frequency discharge plasma effect on conical shock wave: M= 2.5 flow, AIAA J. 41 (2003) 465–469, https://doi.org/10.2514/2.1968.
[19] S. Merriman, E. Ploenjes, P. Palm, I.V. Adamovich, Shock wave control by nonequilibrium plasmas in cold supersonic gas flows, AIAA J. 39 (2001) 1547–1552, https://doi.org/10.2514/3.14899.
[20] G. Schweiger, K. Wanders, M. Becker, Influence of electron-beam-blunt body interactions on density measurements in transition flow, Rarefied Gas Dynamics (1974) 295–303, https://doi.org/10.1016/B978-0-12-398150-9.50034-1.
[21] Y.I. Gerasimov, V.N. Yarygin, A.N. Krylov, Modelling of the flow structure in a composite jet behind two thrusters located near the spacecraft case, Thermophys. Aeromechanics 16 (2009) 375–383, https://doi.org/10.1134/s0869864309030068.
[22] J. Allégre, M. Raffin, A. Chpoun, Rarefied Hypersonic Flow over a Flat Plate with Truncated Leading Edge, Rarefied Gas Dynamics, 1994, https://doi.org/10.1134/s0869864309030068.
[23] A.E. Zarvin, A.S. Yaskin, K.A. Dubrovin, Visualization of low-density gas-dynamic objects in full-scale processes modelling on small experimental plants, Vacuum 3 (2021), 110409, https://doi.org/10.1016/j.vacuum.2021.110409.
[24] J. Allègre, D. Bisch, C. Lengrand, Experimental rarefied density flowfields at hypersonic conditions over 70-degree blunted cone, J. Spacecraft Rockets (1997), https://doi.org/10.2514/2.3300.
[25] M. Belan, S.D. Ponet, D. Tordella, Determination of density and concentration from fluorescent images of a gas flow, Exp. Fluid (2008), https://doi.org/10.1007/s00348-008-0493-5.
[26] J.L. Palmer, B.K. McMillin, R.K. Hanson, Multi-line fluorescence imaging of the rotational temperature field in a shock-tunnel free jet, Appl. Phys. B Laser Opt. 63 (1996) 167–178, https://doi.org/10.1007/bf01095269.
[27] P.C. Palma, P.M. Danehy, A.F.P. Houwing, Fluorescence imaging of rotational and vibrational temperature in shock-tunnel nozzle flow, AIAA J. 41 (2003) 1722–1732, https://doi.org/10.2514/2.7290.
[28] T. Kaseman, L.M. Le Page, S. O'Byrne, Visualization and Thermometry in Hypersonic Wedge and Leading-Edge Separated Flows, 55th AIAA Aerospace Sciences Meeting, 2017, https://doi.org/10.2514/6.2017-0443.
[29] W.J. McCroskey, J.G. McDougall, Shock wave shapes on a sharp flat plate in rarefied hypersonic flow, AIAA J. 4 (1966) 184–186, https://doi.org/10.2514/3.3417.
[30] N. Tsuboi, Y. Matsumoto, Experimental and numerical study of hypersonic rarefied gas flow over flat plates, AIAA J. 43 (2005) 1243–1255, https://doi.org/10.2514/1.10950.
[31] N. Rembaut, R. Joussot, V. Lago, Aerodynamical behavior of spherical debris in the supersonic and rarefied wind tunnel MARHy, J. Space Saf. Eng. 7 (2020) 411–419, https://doi.org/10.1016/j.jsse.2020.07.031.
[32] T.M. Dyer, Upstream influence in a rarefield hypersonic stream, Phys. Fluids 17 (1974) 1535–1538, https://doi.org/10.1063/1.1694930.
[33] F. De Geyter, J.J. Smolderen, J.F. Wendt, Influence of leading-edge geometry on upstream density disturbances in hypersonic flow, in: Rarefied Gas Dynamics, Elsevier, 1974, pp. 335–342, https://doi.org/10.1016/B978-0-12-398150-9.50038-9.
[34] D. Tirumalesa, An experimental study of hypersonic rarefied flow over a blunt body, AIAA J. 6 (1968) 369–370, https://doi.org/10.2514/3.4505.
[35] T. Ozawa, T. Suzuki, K. Fujita, Aerodynamic measurements and computational analyses in hypersonic rarefied flows, AIAA J. 53 (2015) 3327–3337, https://doi.org/10.2514/1.j053889.
[36] T. Ozawa, T. Suzuki, K. Fujita, Investigation of condensation and evaporation effect on CO_2 hypersonic rarefied aerodynamic measurements, in: Emerson Zhang (Ed.), 31st International Symposium, 2019, https://doi.org/10.1063/1.5119538.
[37] C.-W. Wu, C. Liu, D.-L. Hu, H.-L. Liu, H.-J. Huang, Design of a milli-Newton force balance for hypersonic rarefied wind tunnel, Measurement 185 (2021), 110006, https://doi.org/10.1016/j.measurement.2021.110006.
[38] H. Huang, W. Pan, C. Wu, Energy fluctuations in a direct current plasma torch with inter-electrode inserts operated at reduced pressure, Plasma Chem. Plasma Process. 32 (2012) 65–74, https://doi.org/10.1007/s11090-011-9331-2.
[39] H. Huang, W. Pan, Z. Guo, C. Wu, Instabilities in a non-transferred direct current plasma torch operated at reduced pressure, J. Phys. D Appl. Phys. 43 (2010), 085202, https://doi.org/10.1088/0022-3727/43/8/085202.
[40] T. Suzuki, T. Ozawa, K. Fujita, Aerodynamic characteristics evaluation under hypersonic rarefied flow conditions, in: 44th AIAA Thermophysics Conference, San Diego, CA, 2013, https://doi.org/10.2514/6.2013-3019.
[41] G.A. Bird, Molecular Gas Dynamics and the Direct Simulation of Gas Flows, Clarendon Press, Oxford, 1994.
[42] G. Bird, Application of the direct simulation Monte Carlo method to the full shuttle geometry, in: 5th Joint Thermophysics and Heat Transfer Conference, American Institute of Aeronautics and Astronautics, Seattle, 1990, https://doi.org/10.2514/6.1990-1692.
[43] G. Bird, Influence of local configuration on the backflow from small rocket thrusters, in: 28th Aerospace Sciences Meeting, American Institute of Aeronautics and Astronautics, Reno, NV, 1990, https://doi.org/10.2514/6.1990-147.
[44] C. Shen, J. Fan, Z.H. Hu, X.Y. Xu, A new version of position element algorithm of DSMC in calculation of there-dimensional transitional flows, in: C. Shen (Ed.), Rarefied Gas Dynamics, 1997, pp. 162–167.
[45] J. Fan, H.L. Liu, C. Shen, et al., A melecular reflection deterministic criterion used in the position element algorithm of direct statistical simulation, Acta Aerodyn. Sin. 18 (2000) 180–187.
[46] S. Dietrich, I.D. Boyd, Scalar and parallel optimized implementation of the direct simulation Monte Carlo method, J. Comput. Phys. 126 (1996) 328–342, https://doi.org/10.1006/jcph.1996.0141.
[47] H. Liu, in: Muntz Ketsdever, 23rd (Eds.), Validation of a Hybrid Grid Scheme of DSMC in Simulating Three-Dimensional Rarefied Gas Flows, International symposium, 2003, pp. 382–389, https://doi.org/10.1063/1.1581573.
[48] K.C. Kannenberg, I.D. Boyd, Monte Carlo computation of rarefied supersonic flow into a pitot probe, AIAA J. 34 (1996) 83–88, https://doi.org/10.2514/3.13025.
[49] H. Huang, W. Pan, Z. Guo, C. Wu, Laminar/turbulent plasma jets generated at reduced pressure, IEEE Trans. Plasma Sci. 36 (2008) 1052–1053, https://doi.org/10.1109/tps.2004.924577.
[50] W.X. Pan, X. Meng, H.J. Huang, C.K. Wu, Effects of anode temperature on the arc volt–ampere characteristics and ejected plume property of a low-power supersonic plasma, Plasma Sources Sci. Technol. 20 (2011), 065006, https://doi.org/10.1088/0963-0252/20/6/065006.

[51] H. Huang, W. Pan, C. Wu, Arcjet thruster operated with different propellants, IEEE Trans. Plasma Sci. 39 (2011) 2934–2935, https://doi.org/10.1109/tps.2011.2155097.
[52] W.X. Pan, Z.Y. Guo, X. Meng, H.J. Huang, C.K. Wu, Fluctuation characteristics of arc voltage and jet flow in a non-transferred dc plasma generated at reduced pressure, Plasma Sources Sci. Technol. 18 (2009), 045032, https://doi.org/10.1088/0963-0252/18/4/045032.
[53] D. Whitfield, H. Smithson, Low-Density Supersonic Sphere Drag with Variable Wall Temperature, vols. 71–83, AEDC-TR, 1971.
[54] J.H. Ma, A simple formula for the coefficient of spherical drag in hypersonic rarefied airflows, Acta Aerodyn. Sin. (1985) 107–111.
[55] M.I. Boulos, P. Fauchais, E. Pfender, Thermal Plasmas-Fundamentals and Applications, Plenum Press, New York, 1994.
[56] X. Meng, W. Pan, X. Chen, Z. Guo, C. Wu, Temperature measurements in a laminar plasma jet generated at reduced pressure, Vacuum 85 (2011) 734–738, https://doi.org/10.1016/j.vacuum.2010.11.007.
[57] H.-X. Wang, J.-Y. Geng, X. Chen, W.X. Pan, A.B. Murphy, Modeling study on the flow, heat transfer and energy conversion characteristics of low-power arc-heated hydrogen/nitrogen thrusters, Plasma Chem. Plasma Process. 30 (2010) 707–731, https://doi.org/10.1007/s11090-010-9257-0.
[58] W. Pan, X. Meng, H. Huang, C. Wu, Supersonic plasma jets of different gases in low-pressure environment, IEEE Trans. Plasma Sci. 42 (2014) 2450–2451, https://doi.org/10.1109/tps.2014.2320527.
[59] H. Huang, W. Pan, C. Wu, Underexpanded supersonic plasma jet generated by a small arc-heated facility, IEEE Trans. Plasma Sci. 39 (2011) 2882–2883, https://doi.org/10.1109/tps.2011.2153214.